

Deprojection of X-ray data in galaxy clusters: confronting simulations with observations

Kartick C. Sarkar ^{★1}, Arjun Dey ^{†2}, Prateek Sharma ^{‡3}

¹ *Racah Institute of Physics, The Hebrew University of Jerusalem, Israel*

² *Faculty of Physics, Weizmann Institute of Science, Israel*

³ *Department of Physics and Joint Astronomy Program, Indian Institute of Science, Bangalore, India 560012*

22 August 2022

ABSTRACT

Numerical simulations with varying realism indicate an emergent principle – multiphase condensation and large cavity power occur when the ratio of the cooling time to the free-fall time ($t_{\text{cool}}/t_{\text{ff}}$) falls below a threshold value close to 10. Observations indeed show cool-core signatures when this ratio falls below 20–30, but the prevalence of cores with $t_{\text{cool}}/t_{\text{ff}}$ ratio below 10 is rare as compared to simulations. In X-ray observations, we obtain projected spectra from which we have to infer radial gas density and temperature profiles. Using idealized models of X-ray cavities and multiphase gas in the core and 3-D hydro jet-ICM simulations, we quantify the biases introduced by deprojection based on the assumption of spherical symmetry in determining $t_{\text{cool}}/t_{\text{ff}}$. We show that while the used methods are able to recover the $t_{\text{cool}}/t_{\text{ff}}$ ratio for relaxed clusters, they have an uncertainty of a factor of 2 – 3 in systems containing large cavities ($\gtrsim 20$ kpc). We also show that the mass estimates from these methods, in the absence of X-ray spectra close to the virial radius, suffer from a degeneracy between the virial mass (M_{200}) and the concentration parameter (c) in the form of $M_{200}c^2 \approx \text{constant}$. Additionally, lack of soft-X-ray ($\lesssim 0.5$ keV) coverage and poor spatial resolution make us overestimate $\min(t_{\text{cool}}/t_{\text{ff}})$ by a factor of few in clusters with $\min(t_{\text{cool}}/t_{\text{ff}}) \lesssim 5$. This bias can largely explain the lack of cool-core clusters with $\min(t_{\text{cool}}/t_{\text{ff}}) \lesssim 5$.

Key words: galaxies: clusters: intracluster medium – X-rays: galaxies: clusters – techniques: spectroscopic

1 INTRODUCTION

Multi-wavelength observations (e.g., Peterson et al. 2003; Rafferty et al. 2008; Cavagnolo et al. 2008; O’Dea et al. 2008) and numerical simulations (e.g., Sharma et al. 2012; Gaspari et al. 2012; Li et al. 2015; Prasad et al. 2015) have led to a consensus picture of the physics of cool cluster cores. The radio bubbles blown by the active galactic nucleus (AGN) jets powered by accretion onto the central supermassive black hole (SMBH) carve out cavities in X-rays and inject power in the intracluster medium (ICM) comparable to the radiative losses in the core (Churazov et al. 2002; Birzan et al. 2004). Thus the cluster core is in rough thermal balance, and the presence of cold gas can most naturally be understood as a consequence of the nonlinear saturation of local thermal instability in presence of gravity and uplift due to AGN jets. For small density perturbations, cold gas condenses out of the hot ICM if the ratio of the background cooling time to the free-fall time ($t_{\text{cool}}/t_{\text{ff}}$) is smaller than a thresh-

old close to 10 (Sharma et al. 2012; Choudhury & Sharma 2016). For larger $t_{\text{cool}}/t_{\text{ff}}$ only small density/temperature perturbations and internal gravity waves are produced (McCourt et al. 2012; Voit et al. 2017). But nonlinear density perturbations and uplift by jets can produce multiphase gas even for larger $t_{\text{cool}}/t_{\text{ff}}$ (McNamara et al. 2016; Choudhury et al. 2019).

The idealized simulations with heating and cooling balanced in shells are too idealized to compare with observations in detail but provide a useful physical framework of local thermal instability in presence of global thermal balance and background gravity. The biggest shortcomings of this model are the absence of angular momentum and strict thermal balance. Realistic simulations with AGN jets tied to cooling/accretion rate at the center (dominated by the gas in the cold phase) show departure from a perfect thermal balance in the form of cooling and heating cycles (Prasad et al. 2015; Li et al. 2015). Also, because of the small angular momentum imparted by jets, the condensing cold gas has non-zero angular momentum and most of the cold gas circularizes at a radius ~ 1 kpc, much larger than the SMBH sphere of influence. Thus, the question of angular momentum transport and the eventual accretion onto the SMBH, which is crucial for feedback heating, calls for closer scrutiny (e.g., see Hobbs et al. 2011; Gaspari et al. 2013; Prasad et al. 2017).

★ sarkar.kartick@mail.huji.ac.il, kartick.c.sarkar100@gmail.com

† arjun.dey@weizmann.ac.il

‡ prateek@iisc.ac.in

Recent observations (Hogan et al. 2017; Pulido et al. 2018) have very carefully mapped out the gravitating mass distribution in galaxy cluster cores, particularly including the contribution of the brightest central galaxy (BCG) typically found at the centers of relaxed clusters. Accurate determination of the gravitational acceleration (g), and hence $t_{\text{ff}} \equiv (2r/g)^{1/2}$, profile is crucial in testing the $t_{\text{cool}}/t_{\text{ff}}$ models. Earlier models (e.g., Voit & Donahue 2015; Lakhchaura et al. 2016) were not as accurate in calculating the t_{ff} profile close to the center (where $t_{\text{cool}}/t_{\text{ff}}$ is minimum). The key advantage of the Hogan et al. (2017); Pulido et al. (2018) models is that they fix the central potential to be that of an isothermal sphere commensurate with the stellar mass of the central BCG. In other methods, where either only the dark matter halo potential is used or where a parametric form of the potential is not assumed, imposing hydrostatic equilibrium (HSE) can underestimate gravitational acceleration. Additionally, Hogan et al. (2017) find that the number of observed clusters below $t_{\text{cool}}/t_{\text{ff}} \lesssim 10$ is significantly lower than what was found in the numerical simulations (for example Li et al. 2015; Prasad et al. 2018), implying that the real clusters are not cooling as much as in simulations. There could be several possible reasons for such a discrepancy including, but not limited to, some missing physics in the simulations and biases in interpreting the observed spectra. We require detailed analysis of these possibilities to reconcile this discrepancy.

In this paper, we explore the effect of observational biases in interpreting non-hydrostatic atmospheres and realistic simulations. We use different density and temperature distributions – ranging from smooth profiles in hydrostatic equilibrium to very disturbed ICM in jet-ICM simulations – to quantify biases introduced by spectral deprojection and different methods to obtain t_{ff} profiles. We use the mock projected spectra and compare the methods of Hogan et al. (2017, hereafter H17) and Lakhchaura et al. (2016, hereafter, L16) in recovering the input $t_{\text{cool}}/t_{\text{ff}}$ profiles. We also use the data from realistic simulations (Prasad et al. 2015) that include AGN feedback to compare the true $t_{\text{cool}}/t_{\text{ff}}$ profiles against the recovered $t_{\text{cool}}/t_{\text{ff}}$ profiles using the observational/analysis techniques. We also compare methods used by L16 and H17 to recover the $t_{\text{cool}}/t_{\text{ff}}$ profiles and point out their strengths and weaknesses in each of the cases.

The paper is organized as follows. We describe our methods of creating projected spectra from a number of theoretical atmospheres in section 2. Section 3 describes the results of our experiments in each case and provides an overall understanding of biases in recovering t_{cool} and t_{ff} . We discuss the implications of our results in section 4. We finally, present our conclusions in section 5.

2 METHOD

In this paper, we wish to generate mock projected X-ray spectra from theoretical/simulated ICM models and to understand the biases introduced by various assumptions. This is done in four steps. First, projected surface brightness maps and spectra are obtained for a given theoretical/simulated model using a software package called PASS (Sarkar et al. 2017) assuming APEC plasma emission model. The spectra are then divided into different annuli so that each annulus contains a minimum number of counts. Next, we find the average spectrum for each annulus, which is then fitted and de-projected to obtain a radial profile for the electron density and temperature. Finally, the cluster gravitational models and other quantities are reconstructed using these density and temperature profiles. Below we describe these procedures one by one.

2.1 Models

To understand the biases, we consider a variety of toy models as well as realistic simulation data of galaxy clusters. Below we describe each of these models.

2.1.1 Spherically symmetric toy models

These are spherically symmetric models where the density and temperature distributions were obtained by considering the gas to be in hydrostatic equilibrium against the gravitational potential of a central BCG and NFW dark matter distribution. The BCG potential is taken as a singular isothermal sphere with $\Phi = V_c^2 \ln(r/a_0)$, where $V_c = 350 \text{ km s}^{-1}$ and $a_0 = 3 \text{ kpc}$. The dark matter halo mass $M_{200} = 7 \times 10^{14} M_\odot$ and the concentration parameter is 4.7. The entropy profile is taken to be

$$K \equiv \frac{T_{\text{keV}}}{n_e^{2/3}} = K_0 + K_{100} \left(\frac{r}{100 \text{ kpc}} \right)^{1.4} \quad (1)$$

(motivated by Cavagnolo et al. 2009) and $n_e = 7 \times 10^{-4}$ at the outer radius of 500 kpc. For more details of the setup please refer to the initial conditions and parameters described in Prasad et al. (2015, 2018).

We considered two type of models where the $\min(t_{\text{cool}}/t_{\text{ff}}) \approx 12$ and $\min(t_{\text{cool}}/t_{\text{ff}}) \approx 5$. The minimum values were obtained by adjusting the parameter K_0 (the core entropy; 10, 2 keV cm² for the two cases, respectively) in the setup described above. We use these models to test our projection-deprojection tool as well as use them as the default ICM models on which different non-hydrostatic components are added.

2.1.2 Cavity models

Clusters are generally believed to host X-ray cavities, thanks to the activity of an AGN at the BCG. Depending on the accretion rate, orientation and precession of the AGN, the cavities can be of different shapes and sizes. The cavities are believed to be hot but of low density and therefore they appear to be devoid of any X-ray emission. To take into account these effects, we consider a range of simplistic cavity models where the X-ray emission was manually set to be zero inside the spherically symmetric hydrostatic gas distribution.

(i) *Spherical*: These cavities consist of two spherical empty regions, each of radius r_0 and put at $z = \pm r_0$ to represent hot bubbles rising from the central BCG but has not yet disconnected from the center.

(ii) *Displaced spherical*: It is also possible that the AGN has shut off in the recent past leaving behind cavities that have risen up due to buoyancy and lost contact from the center. To mimic such situations, we consider two spherical cavities of radius r_0 centered at $(0, 0, \pm z_0)$.

(iii) *Conical*: These are two conical (right circular) shaped cavities, the symmetry axis of which is lying along the Z-axis with the apex being at $(0, 0, 0)$. These cavities are characterized by their height h_{cav} and half opening angle θ_{cav} .

Detailed values of r_0 , z_0 , h_{cav} , and θ_{cav} in different models can be found in table 2.1. An illustration of the cavity models is also shown in figure 1.

Model Name	Description	Values
sc1a	Spherical cavity with radius r_0 and placed at $z = \pm r_0$; $\min(t_{\text{cool}}/t_{\text{ff}}) \approx 12$	$r_0 = 10$ kpc
sc2a	"	$r_0 = 20$ kpc
sc3a	"	$r_0 = 40$ kpc
cc1a	Conical cavity with half opening angle θ_{cav} and height h_{cav} ; $\min(t_{\text{cool}}/t_{\text{ff}}) \approx 12$	$h_{\text{cav}} = 10$ kpc, $\theta_{\text{cav}} = 30^\circ$
cc2a	"	$h_{\text{cav}} = 20$ kpc, $\theta_{\text{cav}} = 30^\circ$
cc3a	"	$h_{\text{cav}} = 20$ kpc, $\theta_{\text{cav}} = 45^\circ$, $\theta_{\text{view}} = 45^\circ$
bh1a	$\min(t_{\text{cool}}/t_{\text{ff}}) \approx 12$, no cavity, with black hole	$M_{\text{bh}} = 10^{10} M_\odot$
bh2a	"	$M_{\text{bh}} = 10^{12} M_\odot$
cc1b	Conical cavity with $\min(t_{\text{cool}}/t_{\text{ff}}) = 5$	$h_{\text{cav}} = 20$ kpc, $\theta_{\text{cav}} = 30^\circ$
cc2b	"	$h_{\text{cav}} = 20$ kpc, $\theta_{\text{cav}} = 30^\circ$, $\theta_{\text{view}} = 45^\circ$
cc3b	"	$h_{\text{cav}} = 50$ kpc, $\theta_{\text{cav}} = 45^\circ$
cc4b	"	$h_{\text{cav}} = 50$ kpc, $\theta_{\text{cav}} = 45^\circ$, $\theta_{\text{view}} = 45^\circ$
cc5b	"	$h_{\text{cav}} = 50$ kpc, $\theta_{\text{cav}} = 45^\circ$, $\theta_{\text{view}} = 0^\circ$
cc6b	Same as cc4b but the conical cavity is replaced by gas with $T = 7$ keV. This gas follows the HSE pressure profile	$h_{\text{cav}} = 20$ kpc, $\theta_{\text{cav}} = 45^\circ$, $\theta_{\text{view}} = 45^\circ$
dscb	Displaced spherical cavity with $\min(t_{\text{cool}}/t_{\text{ff}}) = 5$	$r_0 = 10$ kpc, $z_0 = 15$ kpc
flr	A floor in the $t_{\text{cool}}/t_{\text{ff}}$ placed at the center	floor ($t_{\text{cool}}/t_{\text{ff}}) = 10$
pr1a	3D geometry with perturbation, $\min(t_{\text{cool}}/t_{\text{ff}}) \approx 12$	$\frac{\Delta\rho}{\rho} _{\text{max}} = 0.01$
pr2a	"	$\frac{\Delta\rho}{\rho} _{\text{max}} = 0.1$
simt0	Simulation data, $\min(t_{\text{cool}}/t_{\text{ff}}) \approx 9.9$	$t = 0$ Myr
simt1000	Simulation data, $\min(t_{\text{cool}}/t_{\text{ff}}) \approx 11$	$t = 1000$ Myr
simt1000th0	Simulation data, $\min(t_{\text{cool}}/t_{\text{ff}}) \approx 11$	$t = 1000$ Myr, $\theta_{\text{view}} = 0^\circ$
simt170	Simulation data, $\min(t_{\text{cool}}/t_{\text{ff}}) \approx 2.4$	$t = 170$ Myr
simt840	Simulation data, $\min(t_{\text{cool}}/t_{\text{ff}}) \approx 3.08$	$t = 840$ Myr
simt1910	Simulation data, $\min(t_{\text{cool}}/t_{\text{ff}}) \approx 3.05$	$t = 1910$ Myr

Table 1. Parameters used in the test models and simulations. The first two letters of each model name (except for ‘flr’ and ‘simt’ models) indicate the geometry of the model while the last letter indicates the $\min(t_{\text{cool}}/t_{\text{ff}})$ of that model (for example, ‘a’ implies $\min(t_{\text{cool}}/t_{\text{ff}}) = 12$ and ‘b’ implies $\min(t_{\text{cool}}/t_{\text{ff}}) = 5$). Unless otherwise mentioned, the viewing angle, $\theta_{\text{view}} = 90^\circ$ (i.e., edge on) by default.

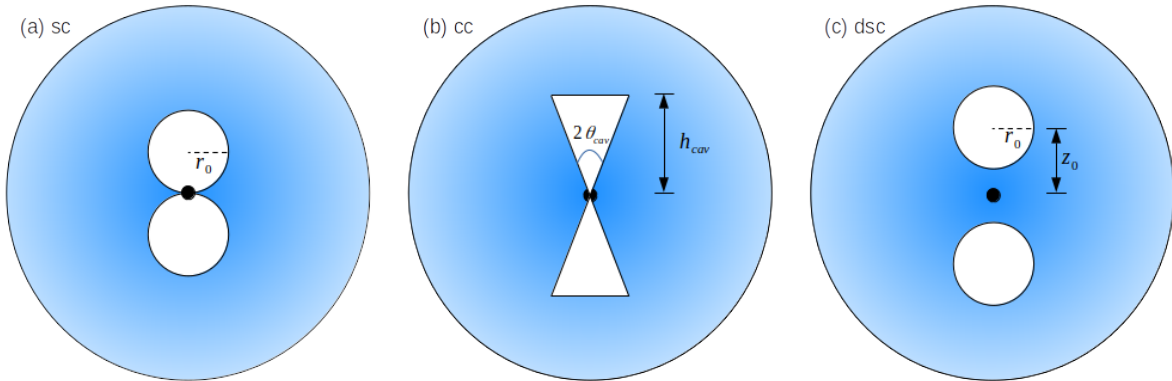


Figure 1. Cartoon diagram of different cavity models considered - (a) spherical cavity models, (b) conical cavity model, and (c) displaced spherical cavity model. The symbols contain the same meaning as in table 2.1.

2.1.3 Black hole potential

Although H17 considered both BCG and NFW potential to construct the hydrostatic equilibrium of clusters, it is also possible that there is an extra potential component that is not closely approximated by the NFW or the isothermal form, e.g., the potential due to the central supermassive black hole. To test this scenario, we consider two cases where a black hole of mass $10^{10} M_\odot$ and $10^{12} M_\odot$ was put at the center of the potential and no cavity was considered. While the latter mass is not a realistic case, it nevertheless can test the dependence on the assumed potential form. The black hole gravity

is given as $g_{\text{bh}} = -GM_{\text{bh}}/r^2$, where, M_{bh} represent the mass of the black hole.

2.1.4 With perturbation

In the case of X-ray analysis, it is known that the observed spectrum biases the phase with higher emission measure (EM) in that particular spectral band. In a realistic cluster where the ICM contains density and temperature fluctuations, the observation may get biased towards a lower temperature (implying higher density at pressure equilibrium) phase. Such situations may underestimate the cooling time (due to higher density obtained) and, therefore, underestimate

the $\min(t_{\text{cool}}/t_{\text{ff}})$ compared to the averaged values at that radius. To check the bias, we seed the ICM with perturbations with the maximum perturbation amplitude $(\Delta\rho/\rho)_{\text{max}} = 0.1$ and wavenumbers lying between $8\pi/(1\text{Mpc})$ and $40\pi/(1\text{Mpc})$; the form of these perturbations is somewhat arbitrary but broadly consistent with the volume-filling ICM in simulations/observations which show $\delta\rho/\rho < 1$; e.g., see [Zhuravleva et al. 2014](#). The way to generate the perturbation field is described in section 4.1.2 of [Choudhury & Sharma \(2016\)](#). The mean value of the $t_{\text{cool}}/t_{\text{ff}}$ ratio is, however, kept to be the same as the toy models considered previously.

2.1.5 Floor in $\min(t_{\text{cool}}/t_{\text{ff}})$

As shown by [Panagoulia et al. \(2014\)](#) and H17 that the cool-core clusters often show an entropy profile $\propto r^{2/3}$ in the central region indicating an expected floor in the $t_{\text{cool}}/t_{\text{ff}}$ profile rather than a typical minimum¹ However, H17 does not find any such floor in the deprojected $t_{\text{cool}}/t_{\text{ff}}$ profiles of the clusters that show a $r^{2/3}$ entropy profile. They attributed this discrepancy to possible large density inhomogeneity towards the smaller radii. To test this hypothesis, we also consider a case where we set the central entropy profile such that it represents a floor of $t_{\text{cool}}/t_{\text{ff}} = 10$. To generate this profile, we assume the same outer entropy profile as our previous models (Eq. 1 with $K_0 = 10 \text{ keV cm}^2$). However, within the radius at which $t_{\text{cool}}/t_{\text{ff}}$ falls below 10, we impose $t_{\text{cool}}/t_{\text{ff}} = 10$ rather than the assumed entropy profile.

2.1.6 Realistic simulations

Apart from considering simplistic toy models, we also consider 3D simulation results to understand the bias in a realistic environment. A brief description of the simulation is given here, but the reader is directed to [Prasad et al. \(2015, 2018\)](#) for more details. Basically, these idealized, isolated ICM simulations start with initial conditions as described in 2.1.1 but evolve the ICM self consistently in presence of radiative cooling and a simple model of AGN feedback. The cluster core is regulated in form of cooling/feedback-heating cycles whose properties are governed by the feedback efficiency and the halo mass. The cores deviate from spherical symmetry during the heating phases when jets/bubbles are prominent.

Detailed values of the parameters and description of the above described models and simulations can be found in table 2.1.

2.2 Projection tools

The models above are projected using the Projection Analysis Software for Simulation (PASS²; [Sarkar et al. 2017](#)) to obtain the surface brightness and X-ray spectrum at different lines of sight and from different angles. We assume the gas to follow APEC plasma model ([Smith et al. 2001](#)) for the emission. Unlike the observed clusters which lie between a redshift of $\approx 0.03 - 0.5$, the test clusters are put at a redshift of 0.001 to avoid limitations due to photon statistics. A much lower redshift gives us a larger number of photons compared to the actual observations of clusters at higher redshifts, and therefore, may suffer from photon statistics (due to low photon count). It becomes necessary for the observations to keep both the energy and

the spatial resolutions coarse to maintain a high photon count in the spatial and energy bins. Therefore, for the majority of the cases we consider here, we keep the cluster at a much low redshift to remove such limitations. In section 4.3 we show the implications of putting the cluster at a typical redshift.

Once projected spectra are obtained, they are then divided into different radial bins to obtain an average spectrum for each annulus. These average spectra are then used to obtain a radial profile for the electron density and temperature. In actual observations, this division is done based on a minimum number of counts per annulus so that each spectrum contains enough photons for a reliable spectral analysis. Since our test clusters are so close and bright, our spectral fits are only very slightly dependent on the total number of photons in the spectrum. We still consider a minimum number count per annulus as a criterion to divide the spectra into radial bins. While making the radial bins, we consider a minimum count of 10^7 photons in each bin assuming an effective area, $A_{\text{eff}} = 100 \text{ cm}^2$ and for an exposure time, $t_{\text{exp}} = 100 \text{ ksec}$ (typical for Chandra observations). The average flux is then calculated in units of photons $\text{s}^{-1} \text{ cm}^{-2} \text{ keV}^{-1}$ after multiplying with the solid angle of the radial bin. This is the flux that we fit in XSPEC. While fitting in XSPEC, we further assume that the instrumental response function (RSP) is a unit matrix, i.e., photon flux directly converts into counts. We use the `flux2xsp` command in XSPEC to generate the `.pha` and `.rsp` files. For the calculations presented here, we do not consider photon statistics and only assume a fixed 1% error in the photon counts. We study the dependence of our results on the bin sizes and realistic photon statistics in section 4.3.

2.3 Deprojecting the data

Once the spectra have been radially binned, they are then deprojected using a similar method as presented in DSDEPROJ ([Sanders & Fabian 2007; Russell et al. 2008](#)).

This deprojection method is based on the assumption of spherical symmetry. As in [Kriss et al. 1983](#), the surface brightness image is divided into concentric circular rings with decreasing radius r_1, r_2, \dots, r_n (i.e., $r_i > r_{i+1}$). The actual three dimensional cluster is assumed to be consisted of spherical shells whose radii are equal to the concentric circular rings. The volume emissivity throughout one such shell is then assumed to be constant. Therefore, the surface brightness, $S_{i,i+1}$ (cts $\text{s}^{-1} \text{ arcmin}^{-2}$) and the emission density $C_{j,j+1}$ (cts $\text{s}^{-1} \text{ cm}^{-3}$) inside the annulus bounded by r_i and r_{i+1} depend on each other through the following relation:

$$S_{i,i+1} = \frac{b}{A_{i,i+1}} \sum_{j=1}^i C_{j,j+1} [V_{j,i+1} - V_{j+1,i+1} - V_{j,i} + V_{j+1,i}] \quad (2)$$

where, $A_{i,i+1} = \pi(r_i^2 - r_{i+1}^2)$ is the area of the bin on the sky bounded by r_i and r_{i+1} , $b = (\pi D/10800)^2$, D is the distance to the cluster in cm and $V_{m,n} = 4\pi/3 \times (r_m^2 - r_n^2)^{3/2}$ for $m < n$ and 0 otherwise.

We can now start from the outermost annuli and find $C_{j,i}$ values for all the shells assumed. Here, we should mention that unlike DSDEPROJ we do not need to subtract the background error because we are deprojecting modeled/simulated data.

Once the spectra of all the shells have been deprojected, we fit it with XSPEC assuming a single temperature APEC model and obtain the temperature and normalization for a known metallicity. This normalization is then used to find the density of gas inside each

¹ For entropy, $S \propto r^{2/3}$, the temperature, $T \propto n_e^{2/3} r^{2/3}$. Now since, $t_{\text{cool}} \propto T/(n_e \Lambda)$ and $t_{\text{ff}} \propto \sqrt{r/g}$, where, $g \sim P/(n_e r) \propto T/r$, it can be shown that $t_{\text{cool}}/t_{\text{ff}} \propto 1/\Lambda$ which is roughly independent of the radius.

² PASS is available freely from <https://github.com/kcsarkar>

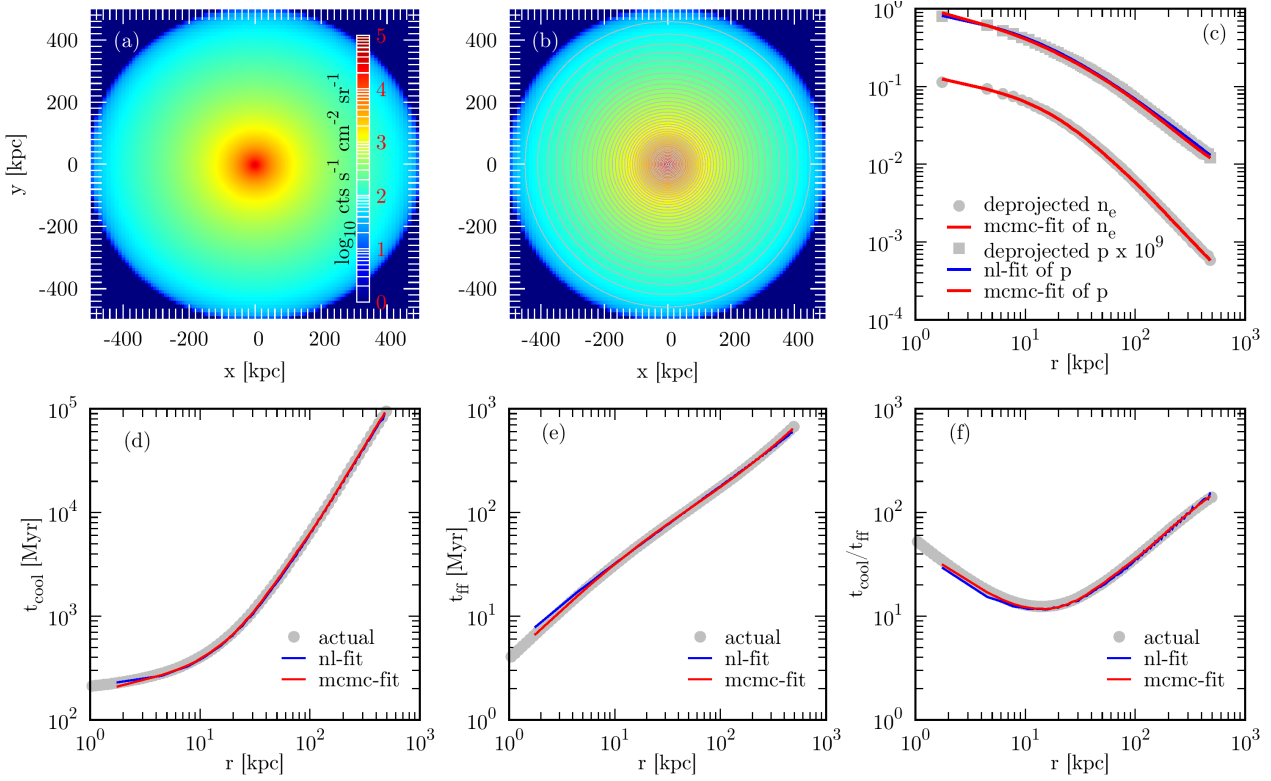


Figure 2. Testing the projection, deprojection, and reconstruction method for a 1-D (spherically symmetric) model without any cavity as described in 2.1.1. (a) Projected surface brightness map in 2.0 – 14.0 keV using `PASS`. Although the brightness is given in actual units, remember that this cluster is placed at a redshift of 10^{-3} and therefore, appears to have an unrealistically high surface brightness. If put at higher redshifts, this cluster would have a much more realistic absolute surface brightness. (b) Annuli considered for deprojecting the spectra. We only plot every 3rd annulus considered originally to increase visibility. (c) Deprojected electron density (n_e) and pressure (p) profiles, along with the fits obtained for them in the two fitting methods considered. The bottom panels show the inferred properties *viz.*, t_{cool} (panel d), t_{ff} (panel e) and $t_{\text{cool}}/t_{\text{ff}}$ (panel f), and their theoretical values (gray points).

spherical shells using the following relation

$$\text{Norm} = \frac{10^{-14} \int n_e n_H dV}{4\pi(D_A[1+z])^2} = \frac{10^{-14} n_e n_H \int dV}{4\pi(D_A[1+z])^2}, \quad (3)$$

where z is the redshift, D_A is the *angular diameter distance*, n_e and n_H are electron and hydrogen densities in cm^{-3} , respectively. We use these quantities in the next step of our analysis.

2.4 Reconstruction

After the deprojected density and temperature profiles have been obtained, we can easily estimate the cooling time as

$$t_{\text{cool}} \approx \frac{3}{2} \frac{nk_B T}{n_e n_i \Lambda(T, Z)}, \quad (4)$$

where $\Lambda(T, Z)$ is the cooling efficiency taken from [Sutherland & Dopita \(1993\)](#)³, $n = \rho/(\mu m_p)$ is the total particle density, $n_e = \rho/(\mu_e m_p)$ is the electron number density, $n_i = \rho/(\mu_i m_p)$ is the total ion number density; we choose $\mu = 0.598$, $\mu_e = 1.151$, $\mu_i =$

³ More recent cooling curves, such as in `CLOUDY-17` ([Ferland et al. 2017](#)) show significantly lower cooling rates for $T \lesssim 10^6$ K and for lower metallicity (see figure A1). This discrepancy, however, is only ≈ 1.5 for $10^6 - 5 \times 10^6$ K gas, above which the discrepancy is even lower. Thus, considering new cooling rates will not change our results much since the plasma in our toy models and simulations has temperature $T \gtrsim 10^7$ K.

1.248. We take these parameters to be constant throughout our calculation. In reality, the values of μ , μ_e , and μ_i remain practically constant for $T \gtrsim 10^5$ K gas and for a large range of metallicities. The metallicity is considered to be $0.2 Z_\odot$ for all the toy models including the simulations. We also show in figure 10 that we are able to recover the profiles quite well even for a higher metallicity. A higher metallicity generally decreases the cooling time of the ICM but this decrease is not more than by a factor of 2 for $T \gtrsim 1$ keV (see fig A1).

The free-fall time is given by

$$t_{\text{ff}} \approx \sqrt{\frac{2r}{g}}, \quad (5)$$

where g is the gravitational acceleration at radius r . However, obtaining t_{ff} requires the assumption of hydrostatic equilibrium in the cluster despite the presence of cavities and non-axisymmetric features in many of the observed clusters.

We follow the traditional methods to obtain t_{ff} from the deprojected profiles to test the accuracy of these methods. We consider two methods to obtain g for each of the scenarios. In the first method, the deprojected pressure ($p = n k_B T$; $n = \mu_e n_e / \mu$) is fitted with a broken power law of the form

$$P(r) = \frac{P_0}{\left(\frac{r}{a}\right)^{\alpha_1} + \left(\frac{r}{a}\right)^{\alpha_2}} \quad (6)$$

and then the derivative of the pressure is used to obtain the gravita-

tional acceleration since in hydrostatic equilibrium,

$$g(r) = -\frac{1}{\rho} \frac{dP}{dr}. \quad (7)$$

(Lakhchaura et al. 2016). This method will be referred to as *nl-fit* (nonlinear fit) from here on.

The second method follows the reconstruction of the hydrostatic equilibrium in each of the deprojected shells by assuming a global $g(r)$ profile for the dark matter and a known BCG. Considering the temperature of the shell and assuming pressure continuity across the shell boundaries, the hydrostatic equilibrium can be solved given the density at the inner shell boundary. For example, if the temperature of a shell bound by r_i and r_{i+1} is taken to be a constant (T_i) and the density at r_i is n_i , then given a gravitation acceleration $g(r)$, one can write down the density at r_{i+1} to be

$$n_{i+1} = n_i \exp\left(-\frac{\mu m_p}{k_B T_i} \int_{r_i}^{r_{i+1}} g(r) dr\right). \quad (8)$$

Note that, although the pressure remains continuous across the shell boundaries, the density and temperature (which is stepwise constant) do not. Once the pressure and the density profiles have been reconstructed, the free parameters of the gravitational potential, *viz.* the virial mass M_{200} and the concentration parameter c can be found by fitting the obtained density profiles to the deprojected ones. The gravitational acceleration, $g(r)$, is assumed to be a combination of the dark matter profile (assumed NFW), a central BCG profile and acceleration due to the SMBH (if any). The NFW gravity profile is taken to be

$$g_{\text{nfw}}(r) = -\frac{G M_{200}}{f(c) r_{200}^2} \times \frac{1}{x^2} \left[\log(1 + cx) - \frac{cx}{1 + cx} \right] \quad (9)$$

where, $x = r/r_{200}$, $r_{200} = \left(\frac{3M_{200}}{200 \times 4\pi\rho_c}\right)^{1/3}$ is the virial radius and $\rho_c = 8.64 \times 10^{-30}$ g is the critical density of the universe at redshift zero, and $f(c) = \log(1 + c) - c/(1 + c)$. From here onward, we will call this method as *mcmc-fit* (since the parameter space of gravitational potential is explored using MCMC). This method is similar to the one followed by Hogan et al. (2017) except that we use the BCG gravity to be

$$g_{\text{bcg}} = -\frac{v_c^2}{r_*} \quad (10)$$

where, $r_* = \sqrt{r^2 + (0.2 \text{ kpc})^2}$ and $v_c = 350 \text{ km s}^{-1}$ by construction. We also use, in some cases, an additional acceleration from the central SMBH in the form of

$$g_{\text{bh}} = -\frac{G M_{\text{bh}}}{r_*^2}, \quad (11)$$

where M_{bh} is the mass of the SMBH.

2.5 Testing the method

Figure 2 shows a step-by-step procedure (from *a* to *f*) of our analysis performed in this paper. It shows results for a spherically symmetric atmosphere in HSE without any cavity/perturbations (as described in section 2.1.1). We find that both the methods (*nl-fit* and *mcmc-fit*) are equally good at fitting the observed pressure profiles and obtaining the cooling time t_{cool} . *mcmc-fit* is, however, better at reproducing the t_{ff} profile towards the center. This is expected since the total potential at very small radii is dominated by the BCG potential which is a parameter for *mcmc-fit* but is unknown to *nl-fit*. In observations, the BCG potential is obtained by estimating the

stellar mass of the galaxy (Hogan et al. 2017; Pulido et al. 2018). In any case, we note that both the *nl-fit* and *mcmc-fit* are successfully able to retrieve the original profiles to very good accuracy. We, therefore, proceed with the analysis of the toy models/ simulation data as listed in Table 2.1.

3 RESULTS

3.1 The fits

We present results of the fits in Fig. 3 for all the cases mentioned in table 2.1. Note that the pressure is not directly fit in *mcmc-fit*; it only fits the density and the pressure is obtained by multiplying the temperature and density profiles. We notice that the fits are good in both the methods in most of the cases except for tiny differences at very small radii. This difference is due to the presence of cavities in the core that cause the pressure there to become non-smooth and even hard to fit in some cases. The difference, however, is prominent in *bh2a*, *simt1000*, *simt1000th0* and *simt1910* cases (marked by orange background in the figure). In the case of *bh2a* (with a $10^{12} M_{\odot}$ point mass at the center), the *nl-fit* works better as it does not assume a parametric form for the fitted potential and can easily fit an unknown potential. This would also be true for a BCG in case its mass is known inaccurately. In *simt1000*, although the fits are not very good, they roughly recover the trend. The one case, where *mcmc-fit* fails completely is *simt1000th0* (viewing angle along the jet axis) where the deprojected density and hence the pressure goes to zero for $r \lesssim 20$ kpc. This is because, for such a projection, the bubble appears to be a hole at the center which, therefore, causes the deprojection method (Eq. 2; which assumes spherical symmetry) to fail as the surface brightness decreases towards the center instead of increasing. Since the inner slope in *mcmc-fit* is fixed to a known BCG potential *i.e.* a known v_c (equation 10), it does not follow the negative slope of the obtained pressure. On the other hand, the *nl-fit* method being independent of the form of the potential recovers the pressure trend. As we will see later, this badly affects the ability for *mcmc-fit* to estimate t_{cool} . A similar reasoning can also be attributed to the bad fitting of *mcmc-fit* method in *bh2a* case. However, the value of the black hole mass considered in this case is very large compared to realistic SMBHs which usually have masses $\lesssim 10^{10} M_{\odot}$. This example illustrates the fallibility of the *mcmc-fit* methods when the actual potential differs qualitatively from the assumed form.

3.2 Recovering t_{ff}

We also are able to recover the free-fall time, t_{ff} , for most of the cases (see Fig. 4) quite well. As mentioned earlier, the *mcmc-fit* method retrieves the t_{ff} better since we use the correct potential for the BCG in this method. The *nl-fit* method is also able to recover the free-fall time to a good accuracy except in the cases where the deprojected pressure does not follow the assumed pressure profile very well, *i.e.*, when the pressure distribution is disturbed by turbulence or when there is a big cavity in the central region. This is because a central cavity makes the deprojected pressure profile flatter than the correct profile. This leads to an underestimation of gravitational acceleration (g) and, therefore, an overestimation of t_{ff} since $t_{\text{ff}} = \left(-\frac{2\rho r}{dP/dr}\right)^{1/2}$, for example, in *sc2a* and *sim1910*. Although, *sc3a* has a cavity size (40 kpc) bigger than *sc2a* (20 kpc), it recovers t_{ff} better. This is mainly due to a poor pressure fit in *sc2a* which

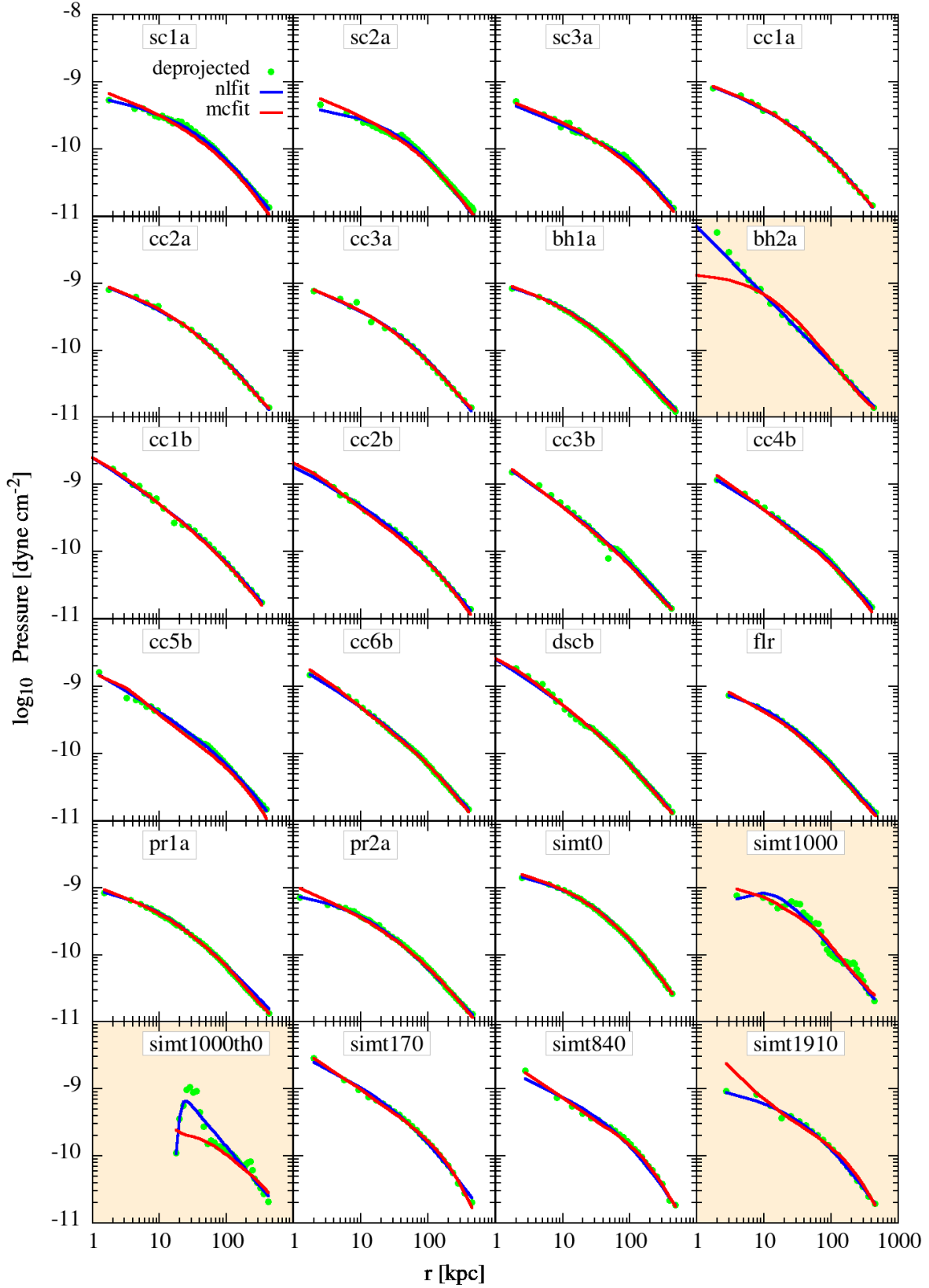


Figure 3. Best fit to the deprojected pressure data points (green points). The solid blue and red lines represent *nl-fit* and *mc-fit*, respectively. Cases that are not fitted well are shown with an orange background. We keep the same orange background in the next few figures for the results obtained from these cases. Note that the effect of cavities in the deprojected ‘sc’ models appears at $r < 2r_0$ because the cavities are placed at $z = \pm r_0$.

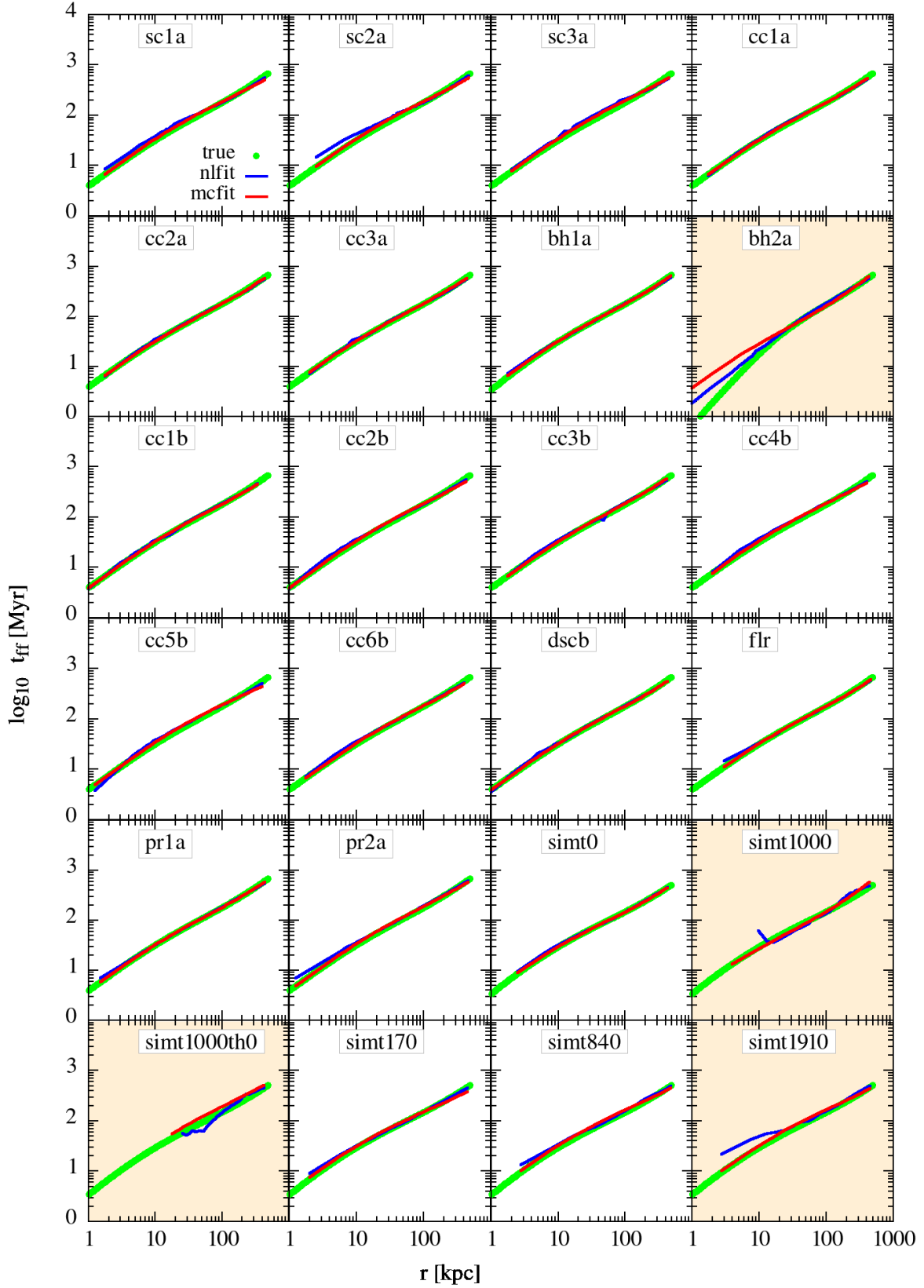


Figure 4. Reconstruction of t_{ff} (equation 5) using the best fit parameters from both the fits. The red and blue lines show the reconstructions for *mlfit* and *nlfit*, respectively. The green circles represent the true free-fall time estimated from the known mass of the toy models/simulations. The panels with orange background represent slightly poor fits as shown in figure 3.

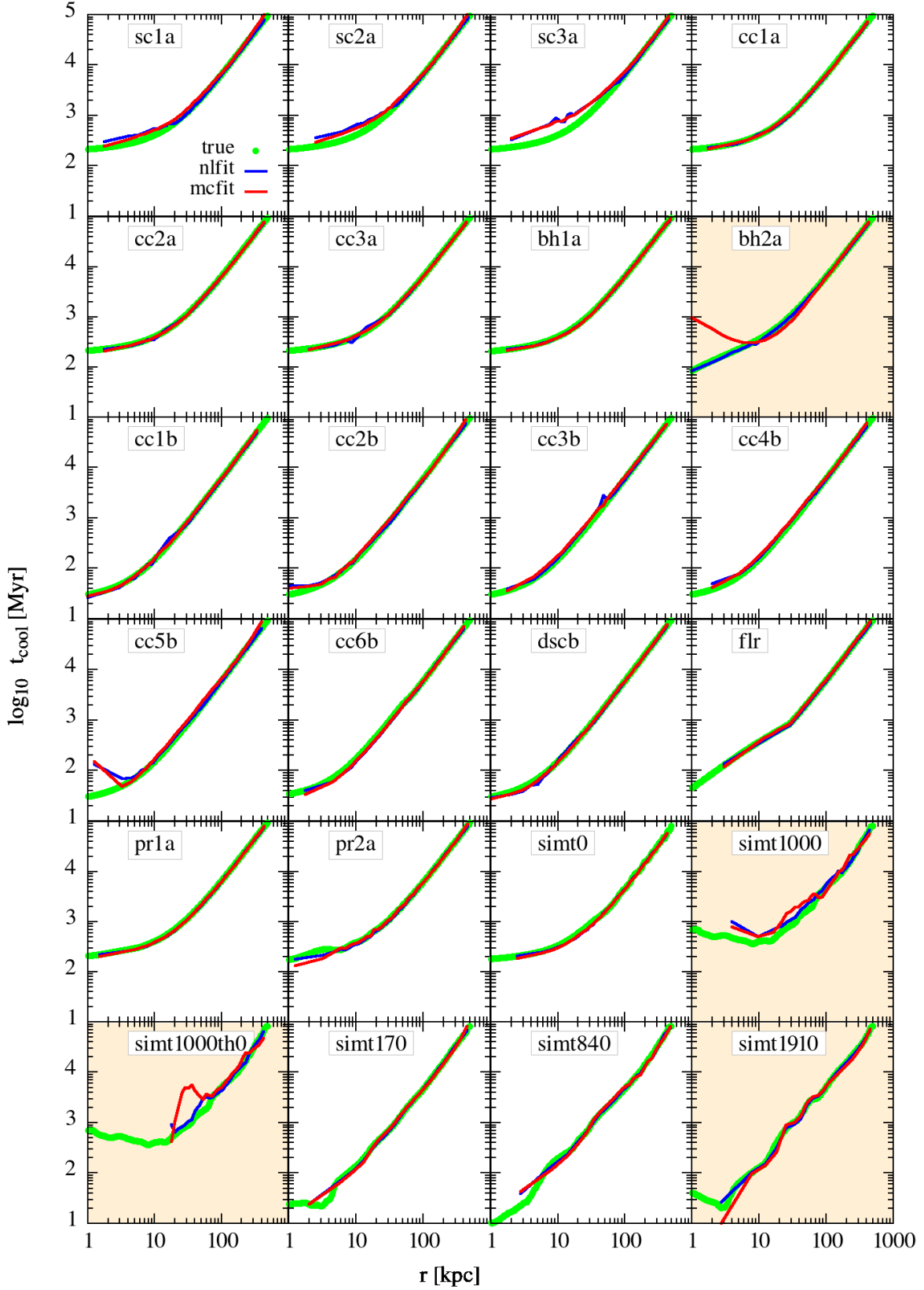


Figure 5. Reconstruction of t_{cool} (equation 4) using the deprojected density and temperatures (in case of *nl-fit*) or using the best fit parameters (in case of *mcmc-fit*). The blue and red lines represent results from *nlfit* and *mcfit* methods, respectively. The green circles are the estimated cooling time from the toy models/simulations as described in Sec. 3.3. The panels with orange background represent cases that have poor fits as shown in fig 3.

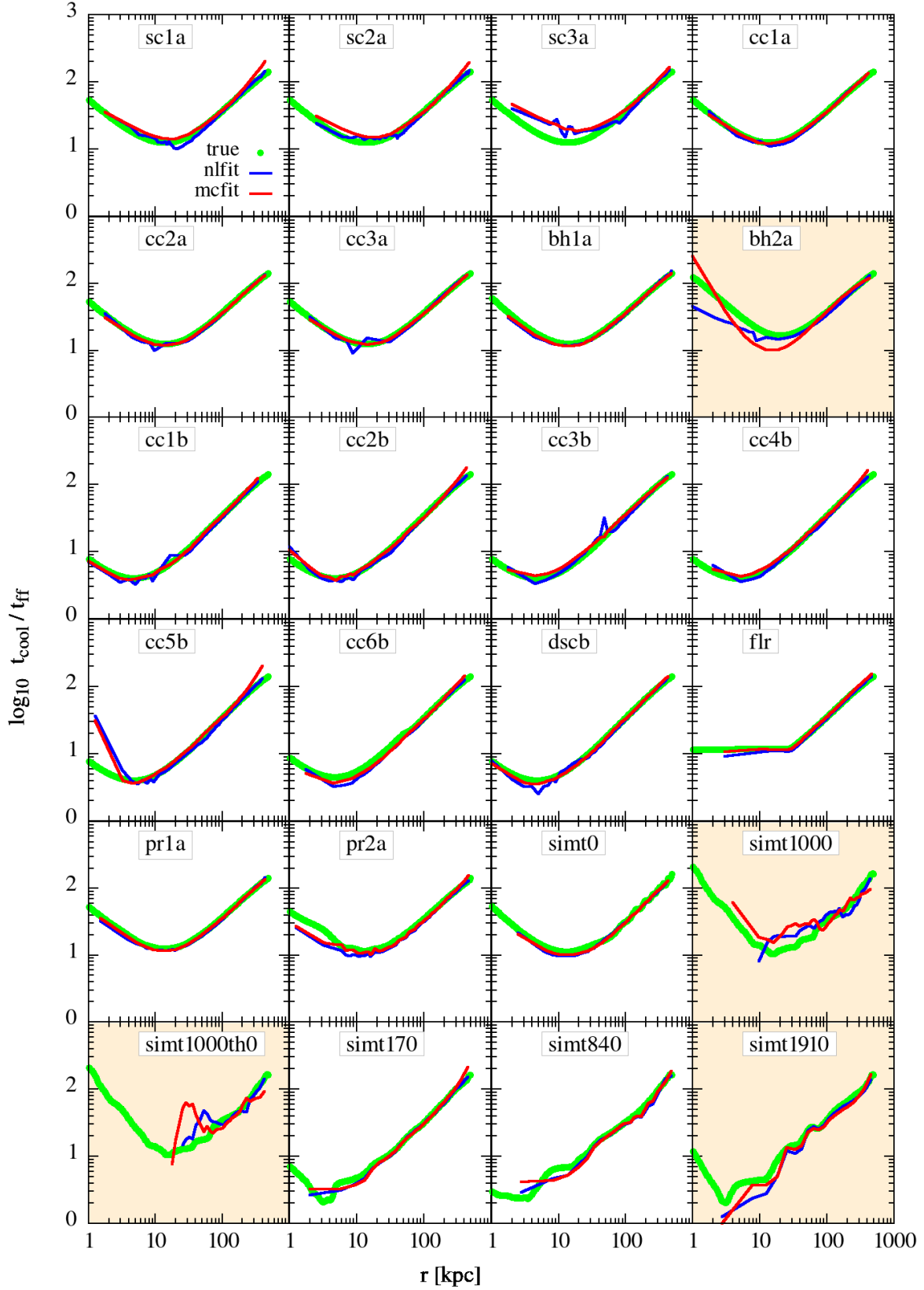


Figure 6. Reconstruction of $t_{\text{cool}}/t_{\text{ff}}$ using the best fit parameters from *nlfite* (blue line) and *mcfite* (red line). The green points are the true $t_{\text{cool}}/t_{\text{ff}}$ ratio of the toy models/simulations.

shows a more prominent kink in the deprojected pressure, leading to a shallower pressure fit.

The figure also shows that, in case of an unexpected gravitational potential at the center, such as *bh2a*, profiles are better fitted by the *nl-fit* method. The *mcmc-fit* method fails to account for the extra potential in such cases. A way to get around this issue in this method could be to allow fitting for v_c . The *nl-fit*, however, proves to be a less effective method at recovering the t_{ff} in the simulated cavity situations (*sim1000*, *simt1000th0*, *sim1910*) than *mcmc-fit* method. We conclude that while estimating t_{ff} , we can use *mcmc-fit* in cases where the central potential is known but should switch to *nl-fit* in the cases where we have limited information on the central potential.

3.3 Recovering t_{cool}

We use the definition of the cooling time as given in equation 4. Note that, while *nl-fit* considers the deprojected n_e and T for calculating the t_{cool} , *mcmc-fit* considers the best fit n_e and the deprojected temperature for this purpose. As we will see later that this is the reason that *nl-fit* can provide a better estimate of t_{cool} than *mcmc-fit*.

We also estimate the average cooling times from the toy models/simulations to compare with the values retrieved from the fitting methods. We estimate the emission weighted density and temperature at each radius and then use these values to obtain the ‘actual’ t_{cool} from Eq. 4. The average density and temperatures are calculated as

$$\begin{aligned} n_{\text{avg}}(r) &= \frac{\int_{\theta, \phi} n \times n_e n_i \Lambda(T, 0.2) dV}{\int_{\theta, \phi} n_e n_i \Lambda(T, 0.2) dV} \\ T_{\text{avg}}(r) &= \frac{\int_{\theta, \phi} T \times n_e n_i \Lambda(T, 0.2) dV}{\int_{\theta, \phi} n_e n_i \Lambda(T, 0.2) dV} \end{aligned} \quad (12)$$

It is clear from the definitions of the n_{avg} and T_{avg} that the cavities containing very low density plasma do not contribute to the averaged quantities.⁴ The definitions are also consistent with the definition of t_{cool} used in the papers reporting numerical simulations of AGN-driven feedback in clusters (for example, Prasad et al. 2018).

The ‘actual’ t_{cool} and the retrieved profiles are shown in Fig. 5. The green points represent the actual t_{cool} , whereas, the solid blue (red) line represents the profiles obtained using the *nl-fit* (*mcmc-fit*) method. Clearly, both methods reproduce the actual t_{cool} profiles quite well in most cases. However, *nl-fit* retrieves t_{cool} better than *mcmc-fit* in general, specifically in the cases where the fit to the deprojected pressure is not good for *mcmc-fit* viz. *bh2a*, *sim1000th0* and *simt1910*. The *nl-fit*, however, shows small bumps in t_{cool} due to the direct use of deprojected density instead of a fitted density. In the presence of a spherical cavity, t_{cool} is overestimated by both methods - the bigger the cavity, the larger is the discrepancy. This is because in observations the density is obtained from the total surface brightness of an annulus and assuming that the emissivity throughout the spherical shell is constant (see 2). This leads to an overall lower density of the shell to match the lower surface brightness. On the other hand, the ‘actual’ t_{cool} obtained from the

models/data using Eq. 12 excludes any cell that has very low emissivity. Therefore, while the information of a cavity is imprinted in the density estimation of *nl-fit* or *mcmc-fit*, the ‘actual’ t_{cool} is not much affected by the presence of cavities. This is the reason that the *nl-fit* or *mcmc-fit* overestimates t_{cool} .

Surprisingly, conical cavity models and the displaced spherical cavity model do not show such an overestimation of the t_{cool} . This is perhaps due to a small solid angle subtended by these cavities leading to a much lower volume occupied by them at any radius compared to the spherical cavities. Since the spherical cavities are connected at the center of the cluster, they can take up almost all the volume at small radii and hence produce relatively low surface brightness. It is, therefore, interesting to also note that for any cluster where the AGN is switched off for a considerable time so that the cavities have risen to a significant distance, the cavities do not much affect the measurement of the t_{cool} . Now, since $t_{\text{cool}} \propto 1/n$ and that the average value of the density due to the cavity is given as $n_{\text{avg}}/n = \cos \theta_{\text{cav}}$ (in an approximate volume averaged sense), one can roughly estimate the effect of such cavities in real observations as $t_{\text{cool,obs}}/t_{\text{cool}} = n/n_{\text{avg}} = 1/\cos \theta_{\text{cav}}$ at any given radius. For example, in case of *sc3a* at $r = 10$ kpc, we estimate that $\theta_{\text{cav}} \approx 70^\circ$ and, therefore, $t_{\text{cool,obs}}/t_{\text{cool}} \approx 3$, roughly consistent with the recovered t_{cool} (see fig 5). On the other hand, the same argument leads to $t_{\text{cool,obs}}/t_{\text{cool}} \approx 1.3$ in the case of *cc3b* where $h_{\text{cav}} = 50$ kpc and $\theta_{\text{cav}} = 45^\circ$.

3.4 Recovering $t_{\text{cool}}/t_{\text{ff}}$

In fig. 6, we plot the recovered $t_{\text{cool}}/t_{\text{ff}}$ from both the methods and compare them with the ‘actual’ $t_{\text{cool}}/t_{\text{ff}}$ profiles obtained from the toy models/simulations. We discuss the results for each subcategory in the following sub-subsections.

3.4.1 Cavity models

As pointed out earlier that both the analysis methods (*nl-fit* and *mcmc-fit*) are able to recover the free-fall time (t_{ff}) in most cases but overestimate the cooling time (t_{cool}) in some cases where there is a cavity subtending a large solid angle present inside the cluster. Clearly, the $t_{\text{cool}}/t_{\text{ff}}$ ratio is also overestimated in those cases. The most prominent example of such a case is the *sc3a* (spherical cavity of size 40 kpc) where $\min(t_{\text{cool}}/t_{\text{ff}})$ is overestimated almost by a factor of 2 – 3. In another example, the methods also overestimate the $t_{\text{cool}}/t_{\text{ff}}$ values within $\lesssim 5$ kpc in *cc5b* (conical cavity of size 50 kpc and viewed down the barrel i.e., $\theta_{\text{view}} = 0^\circ$) due to the projection effects that create a hole in the surface brightness profile. This causes the deprojection method to perform poorly in recovering the density and temperature profiles towards the center. Fortunately, the effect is only noticeable in the very first bin, and therefore, does not affect the minimum value of the $t_{\text{cool}}/t_{\text{ff}}$ which occurs at $r \sim 10$ kpc. Based on the discussion in sections 3.3 and 3.2, we conclude that, in the presence of cavities, the error in $t_{\text{cool}}/t_{\text{ff}}$ ratio is mostly driven by the error in t_{cool} . The recovered $t_{\text{cool}}/t_{\text{ff}}$ ratio differs from the actual $t_{\text{cool}}/t_{\text{ff}}$ if the solid angle subtended by the cavity at the center is large.

3.4.2 Extra potential

As noted in the previous paragraph that the obtained $t_{\text{cool}}/t_{\text{ff}}$ profiles are mostly affected by the estimates of t_{cool} than t_{ff} , since t_{ff} is well estimated in most of the cases. One particular toy model, where the

⁴ While calculating the average quantities, we consider that gas with $T < 0.5$ keV has zero emissivity to avoid any contamination by the cold/warm gas in the estimated quantities. This is done keeping in mind that our method of analysis only uses X-ray data.

estimation of both the t_{cool} and t_{ff} fails in *mcmc-fit* method is *bh2a*. Therefore, the $t_{\text{cool}}/t_{\text{ff}}$ profile also deviates from the true one in this case. On the other hand, *nl-fit* performs much better for this case and recovers the $\min(t_{\text{cool}}/t_{\text{ff}})$ value but deviates from the actual profile within $\lesssim 10$ kpc mostly due to the pressure profile not being a simple double power-law. We should, however, keep in mind that such a massive black hole is not realistic. Any extra potential, if it exists inside the BCG, will either be small (like *bh1a*) where the $t_{\text{cool}}/t_{\text{ff}}$ profiles are recovered very accurately, or will manifest its presence in the observed v_c of the BCG (a parameter in the BCG potential). However, in case the extra potential has a separate profile than the assumed profile of the BCG (either in addition to or instead of), *nl-fit* provides a better way to estimate $t_{\text{cool}}/t_{\text{ff}}$.

3.4.3 With density perturbations

The toy models we considered earlier, have a well defined minimum in the $t_{\text{cool}}/t_{\text{ff}}$ value. Real cool-core systems, on the other hand, may contain perturbations over a smooth distribution either due to the turbulence induced by AGN jets/bubbles or simply due to the non-relaxed nature of the cluster. As a result, these systems may have large density/temperature variations. We mimic such systems with the *pr1a* and *pr2a* models, the results of which are shown in Fig. 6, marked as *pr1a* and *pr2a*. Since the perturbations are added as fluctuations in density (and, therefore, in temperature), which affect the emission measure most, it is not certain that the $t_{\text{cool}}/t_{\text{ff}}$ profile will remain the same. For a better understanding of the systems, we can look into the expected change in t_{cool} (and hence to $t_{\text{cool}}/t_{\text{ff}}$) due to such perturbations. Since the perturbations are added at each radius for a given constant pressure, $nT = n_{\text{avg}}T_{\text{avg}}$ at every radius, $n = n_{\text{avg}}(1 \pm \delta)$, and T are just the local density and temperature. Here, δ is the local density fluctuation. The cooling time therefore, now changes to $t_{\text{cool}} \propto T^{1/2}/n$ (assuming free-free cooling). This allows us to write down the local cooling time as

$$\frac{t_c}{t_{c,\text{avg}}} = \frac{n_{\text{avg}}}{n} \times \left(\frac{T}{T_{\text{avg}}} \right)^{1/2} \approx 1 \pm 3 \frac{\delta}{2}. \quad (13)$$

For example, since the maximum fluctuation of density in *pr2a* is 0.1, we expect about 15% fluctuation on t_{cool} too. Therefore, the maximum deviation of the retrieved t_{cool} (from the ‘actual’ t_{cool}) should also be of a similar order.

Figure 6 shows that both the reconstruction methods are able to recover the actual $t_{\text{cool}}/t_{\text{ff}}$ profiles for these models to a great extent. Although *nl-fit* underestimates $t_{\text{cool}}/t_{\text{ff}}$ in *pr2a* (containing large fluctuations), this is entirely due to the overestimation of the t_{ff} by this method. The *mcmc-fit*, on the other hand, performs much better to estimate the ratio due to the known potential at the center. We, therefore, conclude that as long as the perturbations in the system are small, both the methods work quite well. The recovered $t_{\text{cool}}/t_{\text{ff}}$, however, may be affected only if the amplitude of density fluctuations is $\gtrsim 1$.

3.4.4 Recovering a floor

As mentioned in section 2.1.5, we want to check if we could find a floor in $t_{\text{cool}}/t_{\text{ff}}$ (if it is present) in the core. We find that both the methods are able to recover the floor in $t_{\text{cool}}/t_{\text{ff}}$ (panel *flr* in Fig. 6). Surprisingly, H17 does not find such a floor in their data despite having clusters with entropy $\propto r^{2/3}$ (an indication of a floor in $t_{\text{cool}}/t_{\text{ff}}$) in the inner region, instead, they find a slight upturn in the $t_{\text{cool}}/t_{\text{ff}}$ profile at smaller radii (their figure 7). They argued that

the absence of the $t_{\text{cool}}/t_{\text{ff}}$ floor may be because of the increasing impact of the density inhomogeneity towards the center. In the current analysis we find that the both *nl-fit* and *mcmc-fit* methods are not affected much by the presence of slight density fluctuations but can be seriously affected if the density inhomogeneity is $\gtrsim 1$. However, even if they are affected, the effect has been to flatten out rather than upturn the $t_{\text{cool}}/t_{\text{ff}}$ profile at small radii (see panel *pr2a* in figure 6 and related discussion in section 3.4.3). Therefore, it seems very likely that both the methods would pick up the floor if it is present. This, therefore, means that there is probably no such floor present in the H17 data and that the clusters do not necessarily have to have a floor in $t_{\text{cool}}/t_{\text{ff}}$ even if they have entropy $\propto r^{2/3}$.

Although the above conclusion seems puzzling, the discrepancy can be understood in the following manner. As described by H17 (their section 7), $t_{\text{cool}}/t_{\text{ff}} \propto 1/(T^{1/2} \times \Lambda)$ for an entropy profile, $K \propto r^{2/3}$ (both t_{cool} and t_{ff} are proportional to radius, latter because the potential is close to an isothermal sphere). Here, Λ is the cooling efficiency in units of $\text{erg s}^{-1} \text{cm}^3$. We see that in this case $t_{\text{cool}}/t_{\text{ff}}$ does not directly depend on the radius. However, if the temperature has a radial dependence, it also gets imprinted on the $t_{\text{cool}}/t_{\text{ff}}$ profile. Therefore, we speculate that the absence of a floor in the observed $t_{\text{cool}}/t_{\text{ff}}$ ratio despite the presence of $K \propto r^{2/3}$ entropy profile indicates a temperature variation in that region. It is well known that the temperature decreases towards the center in cool cores. So if the cooling function is flat or has a positive slope (as expected for free-free emission), the $t_{\text{cool}}/t_{\text{ff}}$ ratio is expected to increase inwards in the very center of cool cores.

3.4.5 Simulated cases

In the simulated cases, as already mentioned, although the *mcmc-fit* recovers the t_{ff} better than *nl-fit*, it suffers from poor performance in recovering the cooling time-scale. The overall $t_{\text{cool}}/t_{\text{ff}}$ is still overestimated for some cases in both the methods. As shown in case of *sc3a*, we also find a similar effect of cavity in *sim1000* and even more in *simt1000th0*. Surprisingly, in the cases where the ‘actual’ $t_{\text{cool}}/t_{\text{ff}}$ profile is expected to fall below 5 (cases, *simt170*, *simt840* and *simt1910*), both the methods are able to recover the profile, although not all the way till the center (due to the resolution limit). This may be due to the absence of large cavities since the AGN has not started yet and the cluster is still cooling. We speculate that the effect of cooling phase at the center would be to increase the density and temperature fluctuations, similar to case *pr2a* and, therefore, to affect $t_{\text{cool}}/t_{\text{ff}}$ in a similar way.

A better comparison of both the methods (*nl-fit* and *mcmc-fit*) can be seen in the left panel of figure 7 which compiles the $\min(t_{\text{cool}}/t_{\text{ff}})$ obtained from both these methods and the actual values from simulations. The figure re-iterates the earlier point that both the methods do recover the $\min(t_{\text{cool}}/t_{\text{ff}})$ quite well throughout the duty cycle of an AGN. This means that the discrepancy between the observed and simulated clusters, namely that the simulations show more instances of $t_{\text{cool}}/t_{\text{ff}} \lesssim 10$, may not be due to any bias present in the analysis techniques. However, there may be several other effects, such as the resolution of the central bins and the inability to observe cooler gas, that can affect the estimation of the $\min(t_{\text{cool}}/t_{\text{ff}})$. We address these issues in section 4.

3.5 Recovering the mass profile

Often the recovered $g(r)$ profiles from the analysis methods are integrated to infer the mass profiles of the galaxy clusters since

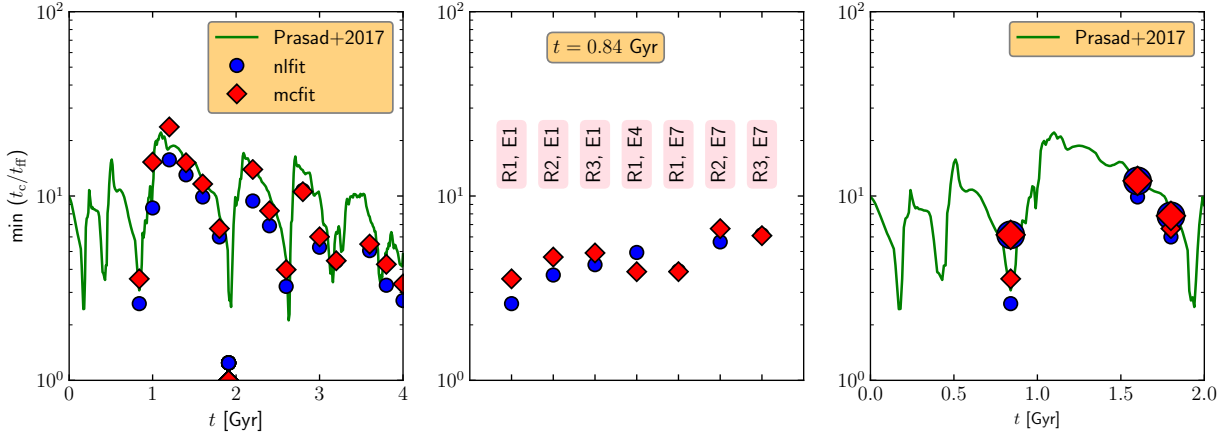


Figure 7. Comparing the $\min(t_{\text{cool}}/t_{\text{ff}})$ recovered from the *nlfits* and *mcfits* fits with the angular averaged values from the simulation. *Left panel:* $\min(t_{\text{cool}}/t_{\text{ff}})$ values obtained at different snapshots of the simulation from theory (green solid line), *nlfits* (blue circles), and *mcfits* (red diamonds). *Middle panel:* $\min(t_{\text{cool}}/t_{\text{ff}})$ values at $t = 0.84$ Gyr for different cases with changing the observed bin-size or the observational spectral energy band. The labels R1 (default resolution), R2, R3 represent the central bin sizes of 2.5, 5.5, and 10 kpc, respectively, and the energy bands E1, E4 and E7 represent 0.1 – 15 keV, 0.4 – 10 keV, and 0.7 – 12 keV, respectively. *Right panel:* the effect of raising the lower energy bound of the observed spectra (shown by larger points). The very low $\min(t_{\text{cool}}/t_{\text{ff}})$ values seem to rise by a factor of 2 – 3, whereas, higher $\min(t_{\text{cool}}/t_{\text{ff}})$ values do not increase significantly.

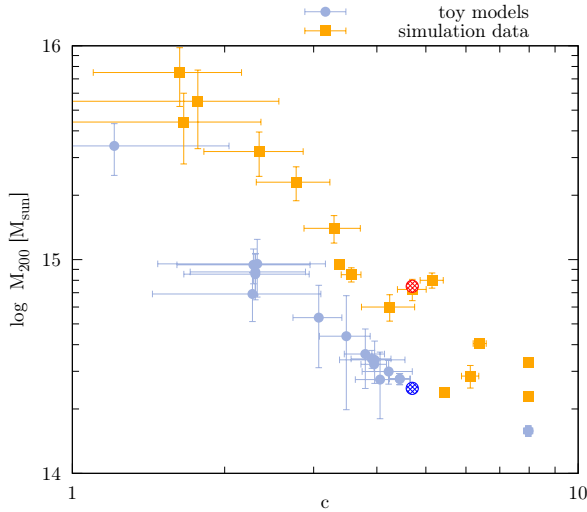


Figure 8. Retrieved virial mass M_{200} and concentration parameter (c) from *mcmc-fit*. The blue hashed circle shows the original value used for these toy models and the red circle represents the value used in the simulation setup. A degeneracy in $M_{200} - c$ is clearly visible in both toy models and the simulation. This is discussed more in section 3.5.

$M(r) = \frac{r^2 g(r)}{G}$. To understand the bias in the process, we plot the obtained virial mass (M_{200}) and the concentration parameter (c) from the *mcmc-fit* for all the toy models and the simulated cases in Fig. 8. The blue points represent all the toy clusters and the orange squares represent the values obtained from the analysis of the simulated data. The hashed blue circle represents the original value used to construct the hydrostatic equilibrium of the toy models, $M_{200} = 2.5 \times 10^{14} M_{\odot}$ and $c = 4.7$. The red empty circle represents M_{200} for the simulations of (Prasad et al. 2018). We find that the recovered values can be off from the actual values almost by a factor of 2–3 in c and by a factor of 5–10 in M_{200} . This also indicates the uncertainty to which we should believe the cluster mass estimation from the spectral observations of the clusters not going close to the virial radius (both our toy models and simulations extend out to 500

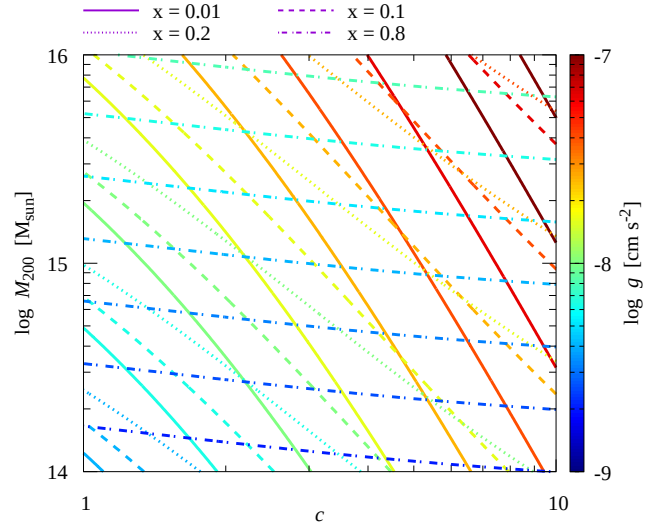


Figure 9. $M_{200} - c$ degeneracy in the NFW profile (9). Different line styles represent different values of $x = r/r_{200}$ and the color of the lines represent the gravitational acceleration, g . Although the degeneracy follows Eq. 14 for $x \ll 1$, it remains a concern even for slightly higher x . The mass uncertainty becomes negligible at $x \sim 1$.

kpc). We stress that, this is due to the systematic uncertainty in the method itself and is very different from the instrumental uncertainties (precision) estimated for the parameters (shown by the error bars against each point). Moreover, there is a systematic degeneracy between the virial mass and the concentration parameter, *i.e.*, $M_{200}c^2 \sim \text{const}$. This degeneracy can be anticipated from Eq. 9 for $x \ll 1$ or equivalently, $cx \ll 1$ and considering that $r_{200} \propto M_{200}^{1/3}$.

$$g(x) \propto \frac{M_{200}^{1/3} c}{f(c)} \times \frac{1}{x} \left[\frac{\log(1+cx)}{cx} - \frac{1}{1+cx} \right] \propto M_{200}^{1/3} c \quad (14)$$

where, in the last step we have used $f(c) \propto c$ (roughly valid for $1 < c < 10$). This relation is very close to the obtained degeneracy. It is therefore clear that for X-ray data only going out to small $x = r/r_{200}$, such a degeneracy is natural to show up in the mass estimates.

Although, the above estimate is for $x \ll 1$, the clusters considered here have virial radii of ≈ 1300 kpc and ≈ 1900 kpc for the toy models and the simulations, respectively. This means that for toy models, $x < 0.4$ and for the simulated cluster, $x < 0.25$ since we use a box size of 500 kpc. In any case, we find that the above-mentioned degeneracy remains for $x \lesssim 0.2$ but becomes increasingly flatter for higher x . Figure 9 shows the $M_{200} - c$ degeneracy in the NFW potential for different values of the extent of the X-ray data (x ; corresponding to different line-styles) and acceleration (indicated by the color of the lines). We see that the degeneracy changes from $M_{200} c^{2.2} \sim \text{const}$ at $x = 0.1$ to $M_{200} c^{1.7} \sim \text{const}$ at $x = 0.2$ (comparable with fig 8), and finally vanishes at $x \sim 0.8$. We, therefore, suggest caution while interpreting the total mass obtained from the X-ray spectral fitting methods presented in this paper, if there are not sufficient photons received from close to the virial radius.

4 DISCUSSION

4.1 Effect of central resolution

One of the limitations of the observations is the radial bin size over which the spectra are measured. The sizes of the bins are often determined by considering a minimum X-ray count in a bin so that there are sufficient photon statistics for estimating the density and temperature. Given that the $\min(t_{\text{cool}}/t_{\text{ff}})$ often arises within the central ~ 20 kpc, not resolving this region creates a problem specifically for distant clusters. It limits our ability to look into the very central region where t_{cool} may be significantly different from the value at larger radii. To investigate this possibility, we re-do our fits for the *simt840* case but with a larger central bin-size. We increase the central bin size from 2.5 kpc (default; case R1 in fig 7) to 5.5 kpc (case R2) and 10 kpc (case R3). We find that the $t_{\text{cool}}/t_{\text{ff}}$ increases only by a factor of 2 at most (see right panel of fig 7). Given that case R1 is able to recover a $\min(t_{\text{cool}}/t_{\text{ff}})$ value of close to 2-3, we conclude that coarsening the radial bins would not immediately move the cluster above the $t_{\text{cool}}/t_{\text{ff}} = 10$ line. We also notice in the right panel of fig 7 that coarsening the radial resolution has little effect in a state with $5 \lesssim t_{\text{cool}}/t_{\text{ff}} \lesssim 10$. In other words, a $t_{\text{cool}}/t_{\text{ff}} \lesssim 10$ cluster should always be detected as a $t_{\text{cool}}/t_{\text{ff}} \lesssim 10$ cluster.

4.2 Observational energy band

Throughout our paper, we have used spectra with a bandwidth of 0.1 – 15 keV, whereas, most of the analysis of the Chandra spectra is done for the energy range of 0.7 – 12 keV. Ideally, such observational bias can neglect the contribution of the $T \lesssim 5 \times 10^6$ K gas towards overall cooling in that region. Since cooling increases with decreasing temperature in $\sim 10^5 - 5 \times 10^6$ K range (especially in isobaric conditions), missing soft-X-ray photons can underestimate cooling by the lower temperature gas and thus overestimate the $t_{\text{cool}}/t_{\text{ff}}$ ratio.

We perform a few experiments on the simulation data to understand the effect of the observational energy band. We trim the spectra for $t = 0.84, 1.6,$ and 1.8 Gyr (corresponding $\min(t_{\text{cool}}/t_{\text{ff}})$

values are $\approx 3, 12,$ and 6) to 0.7 – 12.0 keV range⁵ and then perform the spectral fitting procedures as described in section 2. We also use a coarse spatial binning to see the combined effect on the $t_{\text{cool}}/t_{\text{ff}}$ values. The result is shown in the right panel of fig 7. It shows that while higher $\min(t_{\text{cool}}/t_{\text{ff}})$ values do not change much due to a coarser spatial binning or a harder spectral energy band, the lower $\min(t_{\text{cool}}/t_{\text{ff}})$ values can be overestimated at most by a factor of 2–3. Our experiments, therefore, suggest that observations in softer x-ray emission ($\lesssim 1$ keV) are required to recover the $\min(t_{\text{cool}}/t_{\text{ff}}) \lesssim 5$ clusters. However, Chandra observations at such low energies are difficult due to a) the contamination that has built on the Chandra optical blocking filters, reducing the effective area for energies less than 1 keV, and b) additional absorption by the foreground.

4.3 Photon statistics and error in real observations

So far, we have not considered realistic photon statistics while fitting the spectra in *xSPEC*, a problem often faced in real observations due to the low number of x-ray photons. To understand what the photon statistics may look like, we perform some tests on our fiducial toy model (as presented in section 2.5) by assuming that the photons are detected through an instrument with an effective area, $A_{\text{eff}} = 100$ cm², exposure time $t_{\text{exp}} = 300$ ksec, and that the photons suffer through Poisson statistics. The statistics is included by switching on *cstat* while fitting in *xSPEC*. The analysis is repeated by assuming a higher metallicity ($Z = 0.6Z_{\odot}$) as well as a realistic redshift ($z = 0.2$) for the cluster. In the high redshift case, we binned the photons in coarser spatial and energy bins due to the low photon count. The results of this experiment are shown in figure 10. In the *nl-fit* method (upper panel), the introduction of *cstat* does not alter the results for the low redshift cases. Additionally, the error bars are also negligible (owing to a large photon count), except at the innermost radius where the error in t_{ff} is slightly higher due to a large cell width to radius ratio. For the high redshift cases, the photon statistics become important even after we bin the data in coarser spatial and energy bins. Fitting the spectra with a low photon number, thus introduces a non-negligible error in both t_{cool} and t_{ff} , which is then propagated to $t_{\text{cool}}/t_{\text{ff}}$ (see sec A for details of the error calculation). The error bars, however, are mostly negligible in t_{cool} and t_{ff} , except at the radius where $t_{\text{cool}}/t_{\text{ff}}$ error can be close to 30%. Overall, The recovered values also follow the actual values quite well.

The uncertainties obtained from *xSPEC* toward the density and temperature are also used in the *mcmc-fit* method to obtain fits for ρ_0 , M_{200} , and c . The introduction of the photon statistics does not significantly improve/worsen the fit for the above quantities, as can be seen from the mean values recovered for t_{cool} , t_{ff} , and $t_{\text{cool}}/t_{\text{ff}}$ (bottom panel of fig 10). The error in ρ_a , M_{200} , and c are also comparable to the fits without the photon statistics ($\sim 10 - 20\%$). The recovered profiles overall track the actual profiles in the toy model. The error bars in the recovered quantities are also $\lesssim 30\%$ except for the innermost radius where the spatial resolution is the main source of error in estimating t_{ff} and $t_{\text{cool}}/t_{\text{ff}}$.

⁵ Although Chandra energy band is $\approx 0.7 - 7$ keV, usually one does not have many photons past 7 keV. Therefore, we do not expect any significant change in the *xSPEC* fits even though we included slightly higher energy bins.

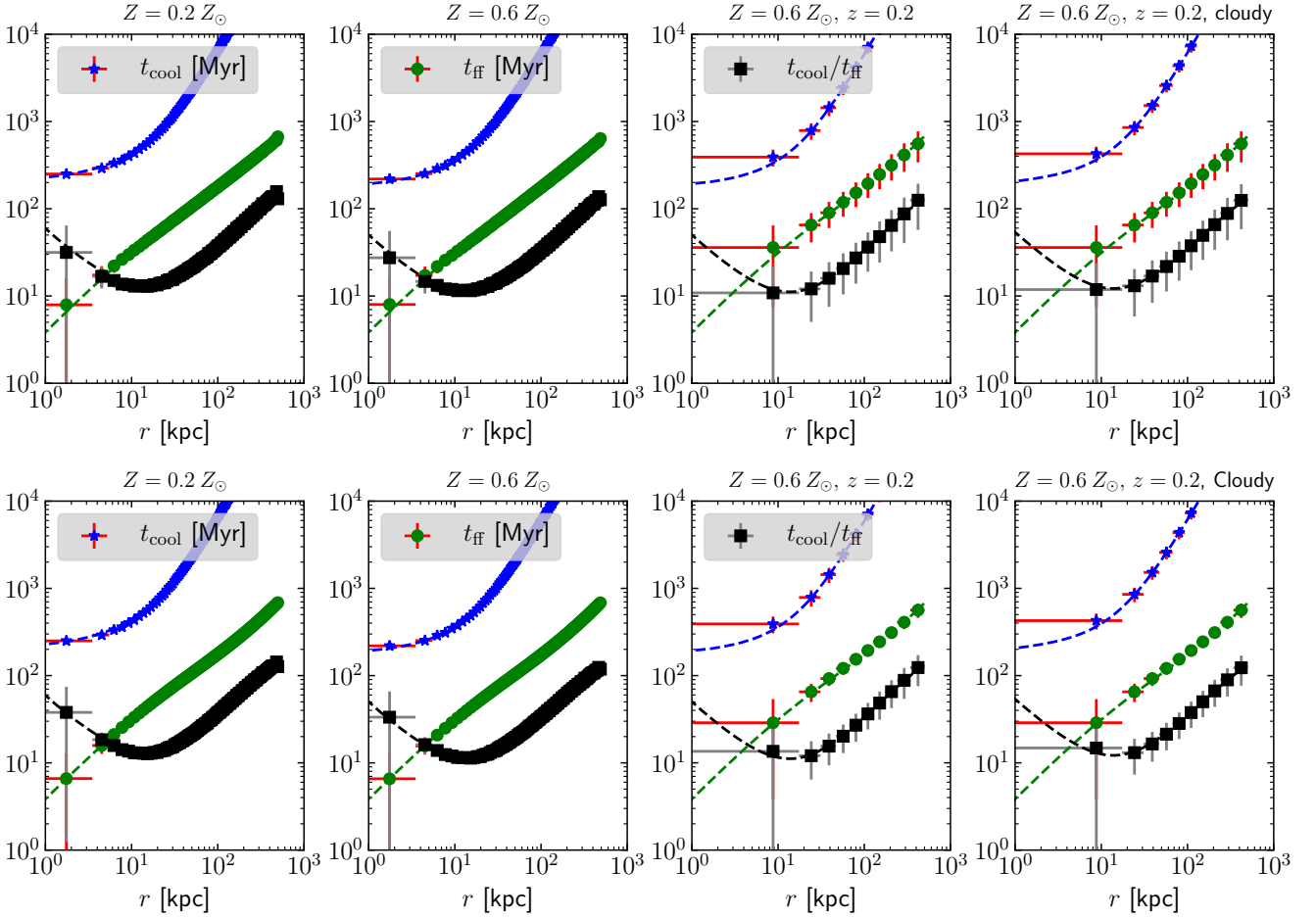


Figure 10. Effects of including realistic photon statistics and redshift in recovering t_{cool} , t_{ff} , and $t_{\text{cool}}/t_{\text{ff}}$. The right column also shows the results if we consider the CLOUDY-17 cooling rates. *Top panels* show the results for the *nl-fit* method and the *bottom panels* show the results for the *mcmc-fit* method. The dashed lines show the actual profiles for the fiducial toy model.

4.4 Discrepancy between observations and simulations

The biases introduced by observational/modeling limitations (limited angular/spatial resolution, lack of soft X-ray spectra, assumed the functional form of the potential, etc.) tend to overestimate $t_{\text{cool}}/t_{\text{ff}}$ by a factor of $\lesssim 3$ in the worst-case scenario that we explore, especially for the smallest $t_{\text{cool}}/t_{\text{ff}}$.

Figure 11 in Prasad et al. (2018) shows a comparison of the distribution of simulated (with and without BCG potential and star formation rate $\sim 5M_{\odot} \text{ yr}^{-1}$) and observed (reported in Pulido et al. 2018) cool core clusters. The observational sample from Pulido et al. (2018) shows 55 clusters and groups with molecular mass between 10^8 and $10^{11}M_{\odot}$, and star formation rate between 0.5 and $270M_{\odot} \text{ yr}^{-1}$. In contrast to simulations, the observed histogram shows a clear lack of systems with $\min(t_{\text{cool}}/t_{\text{ff}}) \lesssim 5$. This may be largely due to the overestimation of $t_{\text{cool}}/t_{\text{ff}}$ in the core because of insufficient spatial resolution (section 4.1) and the lack of soft X-ray spectrum (section 4.2) which mostly affect the coolest cores. The same figure in Prasad et al. (2018) shows that the peaks of the observed and simulated $\min(t_{\text{cool}}/t_{\text{ff}})$ histograms also do not match. The observational peak is narrower and occurs at a slightly higher value ($\min(t_{\text{cool}}/t_{\text{ff}}) \approx 11$) compared to the simulations (NFW potential run peaks at $\min(t_{\text{cool}}/t_{\text{ff}}) \approx 9$ and the NFW+BCG

run has a broad peak between 7 and 11). Thus the observed and simulated X-ray properties of cool cores can be reconciled.

The observational samples of cool core clusters and groups have different selection criteria (e.g., Voit & Donahue 2015; Lakhchaura et al. 2016; Pulido et al. 2018), and the distribution of cool-core properties may differ because of that. But the biggest discrepancy from simulations in most of them is the lack of systems with $\min(t_{\text{cool}}/t_{\text{ff}}) \lesssim 5$, which can be reconciled as discussed in the previous paragraph.

A related recent puzzle is the discovery of a cooling flow in the core of the Phoenix cluster with $\min(t_{\text{cool}}/t_{\text{ff}}) \approx 1$ in its very center (McDonald et al. 2019). How can we explain such a system when observations indicate a general absence of systems having cool cores with $\min(t_{\text{cool}}/t_{\text{ff}}) \lesssim 5$? Phoenix, despite being a high redshift cluster ($z \approx 0.6$), has been observed with an exquisite spatial resolution (it was possible to use two radial bins within 10 kpc; this allowed McDonald et al. 2019 to properly separate the AGN and cluster core emission). Moreover, it is a massive/hot cluster with a peak temperature of ≈ 14 keV. Being hot, the determination of density and temperature in the dense/cool core is not affected as much by the absence of soft X-ray spectra.

Last but not the least, the simulations still very crudely model (or even totally ignore) very important physical processes such

thermal conduction, magnetic fields, angular momentum transport within the central \sim kpc (Gaspari et al. 2013; Prasad et al. 2017), which can affect the distribution of $\min(t_{\text{cool}}/t_{\text{ff}})$. Simulations may not only be missing important physics, but they also have not exhaustively explored various important parameters (such as feedback efficiency).

5 CONCLUSIONS

In this paper, we have studied various models of the intracluster medium using some standard techniques of X-ray spectral analysis. We have created toy models resembling different kinds of non-hydrostatic features such as cavities, inhomogeneities, unknown potential, etc. to create projected X-ray spectra. We then deproject them using often-used tools (especially, Nulsen et al. 2010; Lakhchaura et al. 2016) to recover various physically important quantities such as t_{cool} , t_{ff} and $t_{\text{cool}}/t_{\text{ff}}$. Comparing these recovered quantities with the values from the input models allow us to examine the bias introduced by X-ray observations and the analysis methods. We also use our projection-deprojection method on realistic simulation data to obtain $\min(t_{\text{cool}}/t_{\text{ff}})$ during various stages of AGN activity and compare them with the ratio obtained from observational samples (such as Hogan et al. 2017; Pulido et al. 2018). Below we summarize the main findings of our paper:

- The non-linear fitting method, used by Lakhchaura et al. (2016) and the MCMC method (described by Nulsen et al. 2010) used by more recent studies (such as Hogan et al. 2017) recover the $\min(t_{\text{cool}}/t_{\text{ff}})$ of the non-cooling as well as the cool-core clusters fairly well. The presence of large cavities leads to overestimating the t_{cool} (and hence $t_{\text{cool}}/t_{\text{ff}}$) in both methods. The amount of overestimation depends on the solid angle subtended by the cavity at the cluster center. The *nl-fit* method works better for the systems where the gravitational potential at the center is not known accurately. It also better estimates the cooling time.

- We are able to recover $\min(t_{\text{cool}}/t_{\text{ff}})$ as low as 2–3 by analyzing the simulation data. We, however, find a factor of $\lesssim 3$ overestimation of the $\min(t_{\text{cool}}/t_{\text{ff}})$ if the spatial/angular resolution is $\gtrsim 10$ kpc and if soft X-ray spectrum is not available. The observed lack of cool-core clusters below $\min(t_{\text{cool}}/t_{\text{ff}}) < 5$ (Pulido et al. 2018) compared to the value from AGN simulations may arise due to poor spatial resolution and the lack of soft X-ray spectra. Additionally, there may be additional heating in cool-core clusters that can raise the $t_{\text{cool}}/t_{\text{ff}}$ value above that seen in AGN feedback simulations.

- The estimated cluster mass (M_{200}) from the *mcmc-fit* method suffers from a systematic degeneracy with the estimated concentration parameter, c . Such degeneracy can cause the dark matter mass estimates to be off by a factor of 5 – 10 from the original value and arises purely due to the form of the NFW profile at small r/r_{200} ($\lesssim 0.2$) values. We stress that this degeneracy goes away if one considers the X-ray data for $r/r_{200} \sim 1$ (as used in Nagai et al. (2007)). This also emphasizes the need for X-ray observations from close to the virial radius of a galaxy cluster in order for them to be used as useful cosmological probes, which requires an accurate cluster mass.

This paper, therefore, dives deep into understanding the biases of the analysis methods often used to study the intracluster medium. Although our simplistic toy models may not cover all the possible complications arising in a real ICM, it provides an overall idea of how much various complications can affect the estimated $t_{\text{cool}}/t_{\text{ff}}$

. We hope that the current study will be a useful benchmark to characterize such biases.

ACKNOWLEDGMENT

We thank Nazma Islam for her help in solving technical issues in XSPEC. We also thank the anonymous referee for the helpful comments on the paper. KCS acknowledges support from the Israeli Science Foundation (ISF grant no. 2190/20). PS acknowledges a Swarnajayanti Fellowship (DST/SJF/PSA-03/2016-17) and a National Supercomputing Mission (NSM) grant from the Department of Science and Technology, India.

DATA AVAILABILITY

All the data/codes used in this paper can be found in this paper or under their cited references.

REFERENCES

- Birzan L., Rafferty D. A., McNamara B. R., Wise M. W., Nulsen P. E. J., 2004, *ApJ*, 607, 800
- Cavagnolo K. W., Donahue M., Voit G. M., Sun M., 2008, *ApJ*, 683, L107
- Cavagnolo K. W., Donahue M., Voit G. M., Sun M., 2009, *ApJS*, 182, 12
- Choudhury P. P., Sharma P., 2016, *MNRAS*, 457, 2554
- Choudhury P. P., Sharma P., Quataert E., 2019, *MNRAS*, 488, 3195
- Churazov E., Sunyaev R., Forman W., Böhringer H., 2002, *MNRAS*, 332, 729
- Ferland G. J., et al., 2017, *Rev. Mex. Astron. Astrofis.*, 53, 385
- Gaspari M., Ruszkowski M., Sharma P., 2012, *ApJ*, 746, 94
- Gaspari M., Ruszkowski M., Oh S. P., 2013, *MNRAS*, 432, 3401
- Hobbs A., Nayakshin S., Power C., King A., 2011, *MNRAS*, 413, 2633
- Hogan M. T., et al., 2017, *The Astrophysical Journal*, 851, 66
- Kriss G. A., Cioffi D. F., Canizares C. R., 1983, *ApJ*, 272, 439
- Lakhchaura K., Saini T. D., Sharma P., 2016, *MNRAS*, 460, 2625
- Li Y., Bryan G. L., Ruszkowski M., Voit G. M., O’Shea B. W., Donahue M., 2015, *ApJ*, 811, 73
- McCourt M., Sharma P., Quataert E., Parrish I. J., 2012, *MNRAS*, 419, 3319
- McDonald M., et al., 2019, *ApJ*, 885, 63
- McNamara B. R., Russell H. R., Nulsen P. E. J., Hogan M. T., Fabian A. C., Pulido F., Edge A. C., 2016, *ApJ*, 830, 79
- Nagai D., Vikhlinin A., Kravtsov A. V., 2007, *ApJ*, 655, 98
- Nulsen P. E. J., Powell S. L., Vikhlinin A., 2010, *ApJ*, 722, 55
- O’Dea C. P., et al., 2008, *ApJ*, 681, 1035
- Panagoulia E. K., Fabian A. C., Sanders J. S., 2014, *MNRAS*, 438, 2341
- Peterson J. R., Kahn S. M., Paerels F. B. S., Kaastra J. S., Tamura T., Bleeker J. A. M., Ferrigno C., Jernigan J. G., 2003, *ApJ*, 590, 207
- Prasad D., Sharma P., Babul A., 2015, *ApJ*, 811, 108
- Prasad D., Sharma P., Babul A., 2017, *MNRAS*, 471, 1531
- Prasad D., Sharma P., Babul A., 2018, *ApJ*, 863, 62
- Pulido F. A., et al., 2018, *ApJ*, 853, 177
- Rafferty D. A., McNamara B. R., Nulsen P. E. J., 2008, *ApJ*, 687, 899
- Russell H. R., Sanders J. S., Fabian A. C., 2008, *MNRAS*, 390, 1207
- Sanders J. S., Fabian A. C., 2007, *MNRAS*, 381, 1381
- Sarkar K. C., Nath B. B., Sharma P., 2017, *Mon. Not. R. Astron. Soc.*, 467, 3544
- Sharma P., McCourt M., Quataert E., Parrish I. J., 2012, *MNRAS*, 420, 3174
- Smith R. K., Brickhouse N. S., Liedahl D. A., Raymond J. C., 2001, *ApJ*, 556, L91
- Sutherland R. S., Dopita M. A., 1993, *ApJS*, 88, 253
- Voit G. M., Donahue M., 2015, *ApJ*, 799, L1
- Voit G. M., Meece G., Li Y., O’Shea B. W., Bryan G. L., Donahue M., 2017, *ApJ*, 845, 80
- Zhuravleva I., et al., 2014, *ApJ*, 788, L13

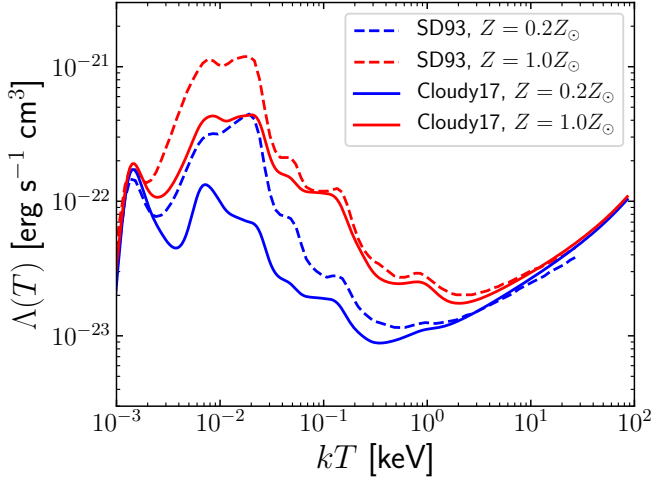


Figure A1. Comparison of the cooling functions of Sutherland & Dopita 1993 (dashed lines) and a more recent cooling curve from CLOUDY-17 (solid lines Ferland et al. 2017). Different colors represent different metallicities. The discrepancy of cooling rates above ≥ 0.5 keV is almost negligible.

APPENDIX A: ERROR CALCULATION

Errors in t_{cool} , t_{ff} , and in $t_{\text{cool}}/t_{\text{ff}}$ ratio are determined numerically from the obtained uncertainties in the fit parameters viz. P_0 , a , α_1 , α_2 , T , and n_e (for *nl-fit*) and M_{200} , c , T , and n_e (for *mcmc-fit*). The numerical uncertainty for any quantity $Q \equiv Q(r, p_1, p_2, \dots)$ is given as

$$\Delta Q = \frac{\partial Q}{\partial r} \Delta r + \frac{\partial Q}{\partial p_1} \Delta p_1 + \frac{\partial Q}{\partial p_2} \Delta p_2 + \dots \quad (\text{A1})$$

where, p_1 , p_2 , ... are the independent parameters and Δp_1 , Δp_2 , ... are the corresponding uncertainties. The derivatives have been calculated numerically.